January 2003

Development of a simple, self-consistent polarizable model for liquid water

Haibo Yu
University of Wollongong, hyu@uow.edu.au

Tomas Hansson
ETH Zurich

Wilfred van Gunsteren
ETH Zurich

Development of a simple, self-consistent polarizable model for liquid water

Abstract

The charge-on-spring method is used to develop a rigid, three-site, polarizable water model, a noniterative and a self-consistent version. In this method, the polarizability is taken into account by a variable separation of charges on selected polarizable centers. One of the pair of polarization charges resides on a polarizable center, while the other one is treated as an additional particle attached to the polarizable center by a parabolic restraint potential. The separation is calculated in response to the instantaneous electric field. We parametrized two models which are based on noniterative and self-consistent versions of the method, respectively. We computed several liquid-phase and gas-phase properties and compared with data available from experiment and ab initio calculations. The condensed-phase properties of both models are in reasonable accord with experiment, apart from discrepancies in electrostatic properties consistent with a slightly too large liquid-state dipole.

Keywords

polarizable, consistent, self, liquid, water, simple, model, development, CMMB

Publication Details

Yu, H., Hansson, T. & van Gunsteren, W. (2003). Development of a simple, self-consistent polarizable model for liquid water. Journal of Chemical Physics, 118 (1), 221-234.

Development of a simple, self-consistent polarizable model for liquid water

Haibo Yu, Tomas Hansson, and Wilfred F. van Gunsteren[a)]
Laboratory of Physical Chemistry, Swiss Federal Institute of Technology Zürich, ETH Hönggerberg, 8093 Zürich, Switzerland

(Received 23 July 2002; accepted 1 October 2002)

The charge-on-spring method is used to develop a rigid, three-site, polarizable water model, a noniterative and a self-consistent version. In this method, the polarizability is taken into account by a variable separation of charges on selected polarizable centers. One of the pair of polarization charges resides on a polarizable center, while the other one is treated as an additional particle attached to the polarizable center by a parabolic restraint potential. The separation is calculated in response to the instantaneous electric field. We parametrized two models which are based on noniterative and self-consistent versions of the method, respectively. We computed several liquid-phase and gas-phase properties and compared with data available from experiment and *ab initio* calculations. The condensed-phase properties of both models are in reasonable accord with experiment, apart from discrepancies in electrostatic properties consistent with a slightly too large liquid-state dipole. © *2003 American Institute of Physics*. [DOI: 10.1063/1.1523915]

I. INTRODUCTION

Most force fields used in biomolecular simulation today describe electrostatic interactions in terms of pairwise additive Coulombic interactions, and thus treat many-body contributions with a mean-field approximation. Such force fields can nevertheless relatively accurately describe bulk liquids, if the parameters in the models are optimized by reference to experimentally determined thermodynamic properties. Because of the biological importance and anomalous physical properties of liquid water, much effort has been directed towards accurate models for water in the liquid state. Many empirical water models, such as SPC,[1] SPC/E,[2] TIP3P, TIP4P,[3] and the recently developed TIP5P,[4,5] SPC/A,[6] and SPC/L,[6] have fixed charges and thus include many-body polarization effects implicitly. They nevertheless reproduce bulk water properties, such as heat of vaporization and density, well. Water molecules in biomolecular systems, however, encounter varying environments, from the mainly hydrophobic binding pockets of receptors where polarization influences are less shielded to the highly solvated surfaces of proteins. Because of the different environments, the degree of polarization of individual water molecules can vary widely across a biomolecular system. In particular, polarization effects play an important part in ionic solvation, where water molecules near the ion will be significantly more polarized than those at a larger distance.[7,8]

One finds in recent literature mainly three different methods used to account for polarization effects in molecular mechanics. The fluctuating charge (FQ) model was proposed by Rick and co-workers.[9,10] In this approach, the size of the atomic partial charges varies in response to the local electric field under a constraint of neutrality. The fluctuating charges are assigned fictitious masses and treated as additional degrees of freedom in the equations of motion. This model does not allow polarization out of the molecular plane, and when applied to liquid water, the FQ model has been found to afford a strongly anisotropic polarizability[9,11] which is at variance with the nearly isotropic experimental value for $\alpha(4\pi\varepsilon_0)^{-1}$ of 1.41 to 1.53×10^{-2} nm^3.[12] To allow the out-of-plane polarizability, this model has been combined with polarizable dipoles,[11,13] which makes it more complicated. A second approach uses point dipoles (PD) (Ref. 14) proportional to an atomic point polarizability and to the electric field at the position $\mathbf{r_i}$ of the point dipole,

$$\boldsymbol{\mu}_i^{\mathrm{ind}} = \alpha_i(\mathbf{E}_i^0 + \mathbf{E}_i^p), \tag{1}$$

where $\mathbf{E}_i^0$ is the field due to the permanent atomic charges and $\mathbf{E}_i^p$ is the field due to other induced dipoles. The electric field can be determined in a self-consistent manner using an iterative procedure or by means of the extended Lagrangian method.[15] Finally the charge-on-spring (COS) model introduced by Straatsma and McCammon[16] is based on modelling the induced dipoles as separations of pairs of point charges. The electric field is allowed to displace one of these point charges, let us call it the "polarization charge," from its equilibrium position according to the polarizability. The COS model circumvents the complex evaluation of dipole–dipole forces since all the electrostatic interactions are point-charge interactions. Therefore, this model can very straightforwardly be combined with the different methods of treating long-range electrostatics, e.g., reaction field, Ewald summation, and particle–particle particle–mesh (P3M) summation methods, which are widely used with pairwise additive force fields. In the article by Straatsma and McCammon[16] a noniterative scheme was described, in which the induced dipoles were determined by the field from the permanent charges of the system only, and the high-order contributions from the induced dipoles were treated in a mean-field approximation by slightly enhancing the partial charges. This simplifies the

a)Author to whom correspondence should be addressed. Electronic mail: wfvgn@igc.phys.chem.ethz.ch Tel: +41-1-6325502; Fax: +41-1-6321039

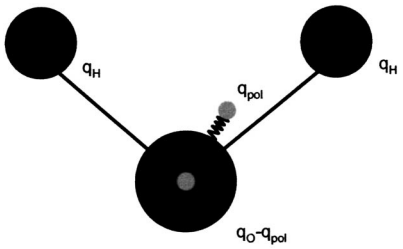

FIG. 1. Interaction sites and geometry of the COS polarizable water models. The models consist of four Coulomb interaction sites located on the oxygen, the two hydrogens and on the polarization charge, plus one van der Waals or Lennard-Jones site located on the oxygen atom. The HOH geometry is rigid, while the polarization charge q_{pol} is connected by a spring to the oxygen which carries a charge $q_{\mathrm{O}}-q_{\mathrm{pol}}$ with $q_{\mathrm{O}}=-2q_{\mathrm{H}}$.

calculations but causes several problems: the energy expression is incorrect, the forces and energies are inconsistent, and the energy is not conserved.

In this paper we will further investigate the COS approach. We start from the noniterative model STR/1 of Straatsma and McCammon[16] and reparametrize it with our standard [GROMOS96 (Refs. 17 and 18)] set of boundary conditions. We then extend it to a self-consistent polarizable water model. Section II introduces the new polarizable water models and gives the simulation details. Results for energies, structures, dynamics, and dielectric permittivity are presented in Sec. III. Finally, in Sec. IV conclusions and an outlook to future water models are given.

II. METHODS

A. Developing the model

We base our models on the COS approach by Straatsma and McCammon.[16] In order to make the model simple, both the noniterative and the self-consistent models retain most of the simplicity of the SPC model[1] (three atomic interaction sites and no van der Waals interactions on the hydrogen atoms). Molecular polarizability will reside on oxygen atoms only, and thus the water model has three atomic centers plus the polarization charge. An induced dipole $\boldsymbol{\mu}_i^{\mathrm{ind}}$ on each oxygen located at $\mathbf{r}_i$ is determined by Eq. (1). As shown in Fig. 1, this dipole is represented by an additional point charge $-q_{\mathrm{pol}}$ on the oxygen and a second point charge q_{pol} which is located at $\mathbf{r}_i'$,

$$\mathbf{r}_i' = \mathbf{r}_i + \frac{\alpha_i}{q_{\mathrm{pol}}}\mathbf{E}_i, \tag{2}$$

where α_i is the molecular polarizability and the electric field $\mathbf{E}_i$ is given by

$$\mathbf{E}_i = \mathbf{E}_i^0 + \mathbf{E}_i^p. \tag{3}$$

In our calculations, q_{pol} is usually $-8.0\,e$. In the polarization model, the additional particle is attached to the polarizable atom with a harmonic bond interaction, with a zero equilibrium distance and a force constant of $q_{\mathrm{pol}}^2/\alpha_i$. If this particle were supposed to move according to Newton's equations of motion, it would also need to have a mass. Because of the added inertia, the polarization charge would then not adjust its position instantaneously to the changing electric field as is required if it is to represent an induced dipole. One way to avoid this would be to energy minimize the positions of the additional particles prior to the evaluation of forces. This would have to be done every dynamics step and would make simulations rather costly. We take an alternative approach. Given a configuration of molecules, the electric field at all polarizable atom positions is evaluated. The electric fields yield new positions for the polarizable charges, according to Eqs. (2) and (3). Since the contribution from the permanent charges will dominate the total electric field, the average effect of polarization due to the other induced dipoles can be combined with the polarization from the permanent charges to save computational effort. This can be seen as analogous to the effective pair potentials in nonpolarizable force fields, in which the average total effect of polarization is represented by modified force field parameters. Straatsma and McCammon[16] thus obtained a noniterative model STR/1 by explicitly treating the first-order polarization, without taking into account the field from the induced dipole moments. In the self-consistent model, however, when calculating the polarization, Eqs. (2) and (3) are iterated until convergence is reached and a self-consistent solution to the equations is found, within the approximation of representing the induced dipoles by separated charges. The intermediate method, i.e., applying the fields from both permanent charges and induced dipoles but only taking one iterative step is inconsistent and was not pursued.

Since the polarization charges are massless, electrostatic forces acting on them cannot be used in the equations of motion, but it is straightforward to add the evaluated forces directly to the forces on the corresponding polarizable atoms and subsequently perform the time step for the atomic centers only. This approximation will be reasonable if the charge separation is small, i.e., if the polarization charge is large. We use a charge of $8\,e$, which is found to be large enough (see discussion below). If, furthermore the location of the polarization charge is stored in the program as a relative displacement from the polarizable center, it will serve as a good first guess for the iterative procedure after the next time step, accelerating the process of attaining self-consistency.

Since induced dipoles are represented by separated charges, an additional term in the potential energy expression is needed, corresponding to the energy cost of distorting the molecule to its polarized state.[2] This energy is given by

$$U^{\mathrm{pol}} = \frac{1}{2}\sum_{i=1}^{N}\frac{\boldsymbol{\mu}_i^{\mathrm{ind}}\cdot\boldsymbol{\mu}_i^{\mathrm{ind}}}{\alpha_i}. \tag{4}$$

Therefore in both, the noniterative and the self-consistent models, the electrostatic interaction energy of the system is of the following simple form:

TABLE I. Parameters of the five SPC-type polarizable water models. For comparison the data for the SPC model are also shown. d_{OH}: OH bond length, ∠HOH: HOH bond angle, q_H: partial charge on the hydrogen, q_O: partial charge on the oxygen, $2q_H=-q_O$, μ^0: fixed molecular dipole moment, q_{pol}: polarizable charge, α: molecular polarizability, C_6: attractive Lennard-Jones coefficient, C_{12}: repulsive Lennard-Jones coefficient. The polarizable water models consist of three atomic centers and one additional polarization charge and are described in Sec. II.

Model	SPC	STR/1	STR/RF	COS/G	COS/B1	COS/B2
Number of force centers	3	4	4	4	4	4
Relative computation cost	1	2	2	4	4	3
d_{OH} (nm)	0.1	0.1	0.1	0.1	0.1	0.1
∠HOH (deg)	109.47	109.47	109.47	109.47	109.47	109.47
$q_H(e)$	0.41	0.351739	0.351739	0.334500	0.344500	0.373000
$q_O(e)$	−0.82	−0.703478	−0.703478	−0.669000	−0.689000	−0.746000
$\mu^0(D)$	2.27	1.95	1.95	1.85	1.90	2.07
$\alpha(4\pi\varepsilon_0)^{-1}$ (10^{-2} nm^3)		0.1445	0.1445	0.14739	0.1401	0.0930
$q_{pol}(e)$		−8.0	−8.0	−8.0	−8.0	−8.0
C_6 (10^{-3} kJ mol^{-1} nm^6)	2.61735	2.61691	2.57013	2.62156	2.61691	2.75691
C_{12} (10^{-6} kJ mol^{-1} nm^{12})	2.63413	3.01500	2.90818	2.96640	3.01500	3.01500

$$U^{ele}=\sum_{i=1}^{N-1}\sum_{j>i}^{N}\left\{\frac{(q_i-q_{pol})(q_j-q_{pol})}{4\pi\varepsilon_0|\mathbf{r}_i-\mathbf{r}_j|}+\frac{(q_i-q_{pol})q_{pol}}{4\pi\varepsilon_0|\mathbf{r}_i-\mathbf{r}_j'|}+\frac{q_{pol}(q_j-q_{pol})}{4\pi\varepsilon_0|\mathbf{r}_i'-\mathbf{r}_j|}+\frac{q_{pol}q_{pol}}{4\pi\varepsilon_0|\mathbf{r}_i'-\mathbf{r}_j'|}\right\}+\frac{1}{2}\sum_{i=1}^{N}\frac{\boldsymbol{\mu}_i^{ind}\cdot\boldsymbol{\mu}_i^{ind}}{\alpha_i},\tag{5}$$

where the summation runs over all polarizable and nonpolarizable atoms or sites. For the latter atoms $q_{pol}=0$ and the last, self-polarization term is zero.

A standard iterative procedure is used to calculate the self-consistent electric fields. On average, two to three iterations are required at every time step to calculate the self-consistent fields with a convergence criterion of

$$\max_{i,x,y,z}(|\Delta E_{i,x}|,|\Delta E_{i,y}|,|\Delta E_{i,z}|)|q_O|d_{OH}<\Delta U,\tag{6}$$

with $\Delta U=2.5$ kJ mol^{-1} and where $\Delta E_{i,x}$, $\Delta E_{i,y}$, and $\Delta E_{i,z}$ are the changes between consecutive iteration steps in the electric field components at oxygen atom i along the x, y, and z axes, q_O denotes the (nonpolarizable part of the) charge of an oxygen atom and d_{OH} is the length of the OH bond. This scheme guarantees that no single water molecule polarization deviates more than ΔU from self-consistency.

B. Simulation methods

A cubic box with a side length of 3.418 nm was filled with 1331 water molecules, resulting in a density of 997.0 kg m^{-3}, which is the experimental value for liquid water at 298 K and 1 atm. Molecular dynamics simulations were performed under NPT conditions with the GROMOS96 (GROningen MOlecular Simulation) package,[17,18] modified to incorporate the polarizable model. The geometries of the water molecules were constrained by applying the SHAKE (Ref. 19) algorithm with a relative geometric tolerance of 10^{-4}. The temperature was weakly coupled to a bath at 300 K with a relaxation time of 0.1 ps (Ref. 20) and the pressure was weakly coupled to a bath at 1 atm with a relaxation time of 0.5 ps (Ref. 20) for which the compressibility of the system was set to the experimental value at 298 K and 1 atm of 7.513×10^{-4} (kJ mol^{-1} nm^{-3})$^{-1}$.[21] This choice of temperature and pressure coupling together with the quoted parameter values has been shown to have a negligible effect on the dynamical properties of liquid water.[20] The equations of motion were integrated using the leapfrog algorithm with a time step of 2 fs. Triple-range cutoff radii of 0.8/1.4 nm were used to treat van der Waals and electrostatic interactions, where the intermediate range interactions were calculated, concurrently to updating the pairlist for short range interactions, every fifth time step. The long range electrostatic interactions beyond the outer cutoff were represented by a reaction field[22,23] with $\varepsilon_{RF}=78.5$. For a comparison of the artifacts of lattice-sum methods such as the Ewald summation and reaction field methods we refer to the literature.[24–31] At the beginning of the simulation the velocities of the atoms were assigned from a Maxwell distribution at 300 K. For every water model, 100 ps of equilibration were followed by 3 ns simulation used for the calculation of the various properties. During the runs, configurations of the system were saved every 0.5 ps.

C. Parametrization

For the noniterative model we started from the STR/1 model of Straatsma and McCammon.[16] Since one of our goals is to achieve consistent results with our [GROMOS96 (Refs. 17, 18)] boundary conditions (triple-range cutoff 0.8/1.4 nm with a reaction field force for long-range electrostatic interactions), we used these boundary conditions in all simulations. We optimized the oxygen–oxygen Lennard-Jones interaction parameters of model STR/RF (Table I) so as to fit the heat of vaporization and the density to the experimental values, while keeping the permanent charges equal to those of STR/1 and assigning the polarizability according to the experimental data. For the self-consistent models, we first aimed at constructing a model (COS/G) with the permanent dipole moment having the gas-phase water value of 1.85 D. Here both the polarizability and oxygen–oxygen Lennard-Jones interaction parameters were varied to fit the heat of vaporization and density to experimental values. Two other models were obtained by increasing the permanent dipole moment beyond the gas-phase value and then varying the polarizability and oxygen–oxygen Lennard-Jones parameters to best reproduce the properties of liquid water.

The heat of vaporization is given by the following formula:[32]

$$\Delta H_{\mathrm{vap}}(T) = -U^{\mathrm{liquid}}(T) + p\Delta V + Q^{\mathrm{int}} + Q^{\mathrm{ext}} = -U^{\mathrm{liquid}}(T) + RT + Q, \quad (7)$$

where ΔH_{vap} is the experimental molar heat of vaporization, U^{liquid} the computed intermolecular potential energy per mole, p the pressure, and ΔV the molar volume change between liquid and gas. R is the gas constant and T is the absolute temperature. Q^{int} and Q^{ext} are quantum corrections: Q^{int} accounts for the difference in vibration energy between water in the liquid and the gas phase. Q^{ext} is a correction due to the intermolecular interaction in the liquid and is the difference in vibrational energy calculated quantum-mechanically and classically. At 300 K this adds up to a total quantum correction of $Q = -0.23$ kJ/mol.[32] The same simulation protocol as described above was used during the parametrization simulations. The initial configuration and velocities for each parametrization run were taken from the last step of 100 ps equilibration of the SPC model. The parametrization simulations were 200 ps long, of which the first 100 ps were treated as equilibration period and excluded from the calculation of averages.

D. Analysis

For each model that was found to achieve reasonable experimental density and heat of vaporization, the following additional properties were evaluated from a 3 ns NPT simulation.

1. Radial distribution function $g(r)$

The structure of liquid water is characterized by a short-range order and a long-range disorder. This is reflected by the radial distribution function $g(r)$, which is experimentally available, for instance, through neutron diffraction. The pair distribution function $g(r)$ gives the probability of finding another atom at a distance r from a given atom, relative to the probability expected for a completely uniform distribution at the same density, and can be calculated by a simple histogram summation in radial shells over all molecules in the system.

2. Self-diffusion coefficient D

The diffusion coefficient is obtained from the long-time limit of the mean square displacement according to the Einstein relation,[33]

$$D = \lim_{t\to\infty} \frac{\langle (\mathbf{r}(t) - \mathbf{r}(0))^2 \rangle}{6t}, \quad (8)$$

where $\mathbf{r}(t)$ corresponds to the position vector of the center of mass at time t, and the averaging is performed over both time and water molecules. In a similar way we can calculate the x, y, and z components of D.

3. Rotational correlation times τ_l^α

Reorientational correlation functions $[C_l^\alpha(t)]$ are calculated for three different axes α: the H–H vector and the O–H vector and the molecular dipole vector $\boldsymbol{\mu}$, according to

$$C_l^\alpha(t) = \langle P_l(\mathbf{e}^\alpha(t)\cdot\mathbf{e}^\alpha(0)) \rangle, \quad (9)$$

where P_l is the Legendre polynomial of order l and $\mathbf{e}^\alpha$ is a unit vector pointing along the α axis in a molecular reference frame. $C_l^\alpha(t)$ shows in general an exponential decay which can therefore be fitted using the following expression:

$$C_l^\alpha(t) = A \exp\left(-\frac{t}{\tau_l^\alpha} \right), \quad (10)$$

where τ_l^α denotes the single-molecule correlation time and A is a constant. The H–H and O–H relaxation can be obtained from ^{1}H–^{1}H and ^{17}O–^{1}H dipolar relaxation NMR experiments, whereas the molecular dipolar orientational correlation function is experimentally obtained from optical measurements such as Raman scattering, fluorescence depolarisation and Kerr relaxation experiments.[34–36]

4. Dielectric permittivity $\varepsilon(0)$

The static dielectric constant or permittivity $\varepsilon(0)$ is calculated from the fluctuations in the total dipole of the simulation box according to a Kirkwood–Fröhlich-type equation derived by Neumann[37]

$$(\varepsilon(0) - 1)\left(\frac{2\varepsilon_{\mathrm{RF}} + 1}{2\varepsilon_{\mathrm{RF}} + \varepsilon(0)} \right) = \frac{\langle \mathbf{M}^2 \rangle - \langle \mathbf{M} \rangle^2}{3\varepsilon_0 V k_B T}, \quad (11)$$

where $\varepsilon_{\mathrm{RF}}$ is the relative dielectric permittivity of the reaction field continuum that is used in the simulation, $\mathbf{M}$ is the total dipole moment of the system, V is the volume of the box, k_B is the Boltzmann constant, T is the absolute temperature, and ε_0 is the dielectric permittivity of vacuum.

5. Debye relaxation time τ_D and frequency-dependent permittivity $\varepsilon(\omega)$

The Debye relaxation time τ_D can be obtained by calculation of the normalized autocorrelation function $\Phi(t)$ of the total dipole moment of the system,

$$\Phi(t) = \frac{\langle \mathbf{M}(0)\mathbf{M}(t) \rangle}{\langle \mathbf{M}^2(0) \rangle}. \quad (12)$$

If one assumes the system to behave like an ideal Debye dielectric, the function $\Phi(t)$ becomes a pure exponential,

$$\Phi_{\mathrm{ex}}(t) = \exp\left(-\frac{t}{\tau_{\mathrm{ex}}} \right). \quad (13)$$

The Debye relaxation time τ_D can then be found using the following relation:[22]

$$\tau_D = \frac{2\varepsilon_{\mathrm{RF}} + \varepsilon(0)}{2\varepsilon_{\mathrm{RF}} + 1}\, \tau_{\mathrm{ex}}. \quad (14)$$

However, in practice the function $\Phi(t)$ as observed from simulations is not a pure single-exponential one. It generally shows an initial fast decay followed by a slower exponential

one. This means that the slow decay is better represented using the following approximation[38] to $\Phi(t)$,

$$\Phi_s(t)=(1-A)(1-H(t))+A\exp\left(-\frac{t}{\tau_s}\right) \tag{15}$$

in which the function $H(t)$ is the Heaviside function, i.e., $H(t)=0$ for $t<0$ and $H(t)=1$ for $t\geqslant 0$. The first term represents the initial decay. Using Eq. (13) the infinite-frequency dielectric permittivity $\varepsilon(\infty)$ equals 1. When approximating $\Phi(t)$ using Eq. (15), this is not true as long as $A\neq 1$.

The frequency-dependent dielectric permittivity $\varepsilon(\omega)$ of the system can be obtained from the normalized autocorrelation function $\Phi(t)$ of the total dipole moment $\mathbf{M}$ of the system, using its Fourier–Laplace transform,[39]

$$\frac{(\varepsilon(\omega)-1)}{(\varepsilon(0)-1)}\frac{(2\varepsilon_{\mathrm{RF}}+\varepsilon(0))}{(2\varepsilon_{\mathrm{RF}}+\varepsilon(\omega))}=\int_0^\infty\left(-\frac{d\Phi}{dt}\right)e^{-i\omega t}dt \tag{16}$$

assuming Debye dielectric behavior after the first initial phase, one has[38–41]

$$\frac{\varepsilon(\omega)-\varepsilon(\infty)}{\varepsilon(0)-\varepsilon(\infty)}=\frac{1}{1+i\omega\tau_D}. \tag{17}$$

Inserting Eq. (15) into Eq. (16) and using Eq. (17) one finds

$$\varepsilon(\infty)=1+\frac{(1-A)(\varepsilon(0)-1)}{1+A\lambda}, \tag{18}$$

$$\tau_D=(1+A\lambda)\tau_s, \tag{19}$$

with

$$\lambda=\frac{\varepsilon(0)-1}{2\varepsilon_{\mathrm{RF}}+1}. \tag{20}$$

Equation (19) and approximation Eq. (15) were used to obtain τ_D.

6. Finite and infinite system Kirkwood factor G_k and g_k

The finite system Kirkwood factor G_k measures the orientational correlation between a single dipole and all its peers. It is determined from

$$G_k=\frac{\langle\mathbf{M}^2\rangle-\langle\mathbf{M}\rangle^2}{N\langle\mu^2\rangle}, \tag{21}$$

where N is the number of molecules and μ is the dipole moment of a single molecule. The finite system Kirkwood factor depends on the boundary conditions ($\varepsilon_{\mathrm{RF}}$) and the box shape. For our simulation conditions, the relation to the infinite system Kirkwood factor g_k,[42] which is available experimentally, is the following:

$$g_k=\frac{(2\varepsilon_{\mathrm{RF}}+\varepsilon(0))(2\varepsilon(0)+1)}{3\varepsilon(0)(2\varepsilon_{\mathrm{RF}}+1)}G_k. \tag{22}$$

7. Heat capacity C_p

The heat capacity at constant pressure can be approximated[32] according to the formula,

$$C_p\approx\frac{U_2^{\mathrm{tot}}-U_1^{\mathrm{tot}}}{T_2-T_1}+\frac{\partial Q^{\mathrm{int}}}{\partial T}+\frac{\partial Q^{\mathrm{ext}}}{\partial T}, \tag{23}$$

where U^{tot} is the total energy per molecule and Q^{int} is the quantum contribution of the intramolecular vibrational modes to the specific heat, while Q^{ext} is the difference between the quantum-mechanical and classical intermolecular vibrational energy. These quantum contributions add up to about $-9.3\ \mathrm{J\,mol^{-1}\,K^{-1}}$ at 298 K and 1 atm. For this purpose, we carried out three additional NPT-simulations of 500 ps each (plus an initial 100 ps of equilibration) at 298, 318, and 338 K, respectively.

8. Thermal expansion coefficient α

The thermal expansion coefficient α is calculated using a finite-difference expression,[43]

$$\alpha=\frac{1}{V}\left(\frac{\partial V}{\partial T}\right)_p\approx-\left(\frac{\ln\left(\frac{\rho_2}{\rho_1}\right)}{T_2-T_1}\right)_p, \tag{24}$$

where ρ_1 and ρ_2 are the densities at the temperature T_1 and T_2, given a constant pressure p. The simulations at different temperatures (referred to above) were used for this purpose.

9. Isothermal compressibility κ_T

The isothermal compressibility κ_T can be obtained[44] by the following finite-difference expression,

$$\kappa_T=-\frac{1}{V}\left(\frac{\partial V}{\partial p}\right)_T=\frac{1}{\rho}\left(\frac{\partial\rho}{\partial p}\right)_T=\left(\frac{\partial\ln(p)}{\partial p}\right)_T\approx\left(\frac{\ln\left(\frac{\rho_2}{\rho_1}\right)}{p_2-p_1}\right)_T, \tag{25}$$

where ρ is the density of the system. For this purpose, we carried out three additional NVT simulations of 500 ps each (plus an initial 100 ps of equilibration) at a density of 947.0, 997.0, and 1047.0 $\mathrm{kg\,m^{-3}}$, respectively.

III. RESULTS AND DISCUSSIONS

In the parametrization procedures, we simulated all the models under NPT conditions and monitored the total potential energy and density (data not shown). After 100 ps, the total potential energies and densities of all the models had converged. The promising models were simulated for 3 ns (after 100 ps equilibration). In this section we will describe the results of production simulations of liquid water with six models, namely, SPC (simple point charge), STR/1 (the noniterative model developed by Straatsma and McCammon[16]), STR/RF (reparametrized STR/1), COS/G (a self-consistent model which reproduces the experimental gas-phase dipole moment), COS/B1, and COS/B2 (self-consistent models which have a bigger permanent dipole than the experimental gas-phase dipole). We make comparisons to data from *ab initio* calculations and experiments where available. Parameters of the six models are shown in Table I.

TABLE II. Thermodynamic properties of the different water models at 300 K and 1 atm, together with the root-mean-square fluctuations in parentheses, obtained as averages over the last 1 ns of the simulations. T: temperature of the simulation, p: pressure, ρ: density, U^{tot}: total potential energy, U^{coul}: Coulomb energy (does not include the U^{pol}), U^{pol}: polarization energy, U^{lj}: Lennard-Jones energy. U^{corr}: polarization correction energy. U^{pol} is calculated according to Eq. (4) while $U^{\mathrm{corr}}=\Sigma_{i=1}^{N}(\mu_i^0-\mu_i^{\mathrm{gas}})^2/2\alpha_i$.[2]

Model	SPC	STR/1	STR/RF	COS/G	COS/B1	COS/B2	Expt
T (K)	302.4(3.5)	299.8(3.39)	299.7(3.48)	309.0(3.57)	309.0(3.64)	302.5(3.54)	300.0
p (atm)	−0.28(177.0)	0.78(232.89)	4.10(233.9)	6.91(226.54)	5.71(236.85)	5.50(233.94)	1
ρ (kg m^{-3})	970.5(5.5)	971.0(4.81)	990.0(4.95)	994.6(5.21)	1004.3(5.24)	992.4(4.79)	997.0[21]
U^{pot} (kJ mol^{-1})	−41.26(0.13)	−40.28(0.16)	−41.69(0.27)	−37.36(0.16)	−40.04(0.17)	−41.73(0.15)	−41.5[32]
U^{coul} (kJ mol^{-1})	−48.23(0.21)	−63.28(0.41)	−66.17(0.40)	−68.62(0.55)	−73.23(0.58)	−63.98(0.40)	
U^{pol} (kJ mol^{-1})	0.0	12.01(0.10)	12.73(0.10)	19.16(0.23)	19.78(0.22)	11.54(0.11)	
U^{lj} (kJ mol^{-1})	6.97(0.12)	10.99(0.28)	11.75(0.18)	12.09(0.21)	13.41(0.22)	10.72(0.18)	
U^{corr} (kJ mol^{-1})	3.74	0.21195	0.21195	0.0	0.09910	0.99523	

A. Thermodynamic properties

The energetic properties and densities of the models are listed in Table II. In agreement with earlier observations, the density of SPC is slightly too low. The fitting procedures of STR/RF and COS/B2 did succeed in finding model parameters that would reproduce both the density and the potential energy. The average pressures are close to 1 atm for all the models, the fluctuations for polarizable water models being larger than for the nonpolarizable SPC model. For the STR/1 model we found a higher potential energy (−40.28 kJ mol^{-1}) than Straatsma and McCammon[16] reported (−41.61 kJ mol^{-1}) and a lower density (971.0 kg m^{-3}) than they reported (994.9 kg m^{-3}). Their results were obtained by simulating a smaller box of 216 water molecules for short periods of 50 ps equilibration and 50 ps production with a shorter cutoff radius of 0.9 nm.[16] We note that for the COS/G and COS/B1 models, the actual temperatures are about 9 K higher than the reference temperature of 300 K of the heat bath, which indicates heating in these simulations. More iterations were needed in the COS/G and COS/B1 simulations than in the COS/B2 one, since the former models have a bigger induced dipole and polarization energy.

In model COS/G, the charges are set to yield the experimental gas-phase dipole moment. Upon varying the Lennard-Jones interactions of the oxygen atoms and the polarizability of the oxygen atoms, we were not able to find a set of parameters for COS/G for which the experimental density and heat of vaporization were attained. In order to investigate this problem, we compared the total dipole moment of the water dimer as a function of oxygen–hydrogen R(OH) distance with the data Alfredsson *et al.*[45] obtained from restricted Hartree–Fock MP4 *ab initio* calculations. Figure 2 shows the relative orientation of the two rigid water molecules which was maintained while varying the distance R(OH). The total dipole moment of the water dimer as a function of the R(OH) distance is shown in Fig. 3. In the COS/G model the total dipole moment of the water dimer is underestimated by about 5% at a distance of 0.6 nm. At such long distances, the total dipole moment will be mainly determined by the permanent dipole since the polarization effect is relatively small (<0.5%). Therefore, the models COS/B1 and COS/B2 were built with enlarged permanent dipole and a smaller polarizability, which yield a bigger total dimer dipole moment at longer distances. In this way, the permanent dipole of the water monomer is bigger than the gas-phase value of 1.85 D. A comparable observation was made in the development of the polarizable water models PPC,[46] POL1,[47] and RPOL.[48] Another reason for which a COS/G-like model cannot reproduce the liquid properties well may lie in the fact that an atom-centered three-point-charge model cannot simultaneously reproduce both the dipole and the quadrupole moment of a water molecule.[49] For example, charges that reproduce the dipole moment of the gas phase lead to a quadrupole moment about 40% smaller than the experimental one.

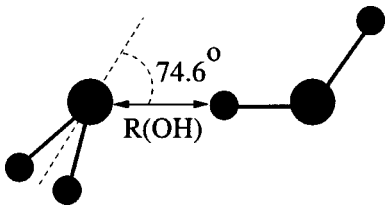

FIG. 2. Geometry of the water dimer for the calculation of the dimer dipole moment: the rigid monomers maintain their relative orientation and were translated along R(OH) only (Ref. 45).

B. Liquid structure

The O–O, O–H, and H–H radial distribution functions (RDF) $g(r)$ are plotted in Figs. 4, 5, and 6 for the SPC, STR/1, STR/RF, COS/B1, and COS/B2 models (dotted lines)

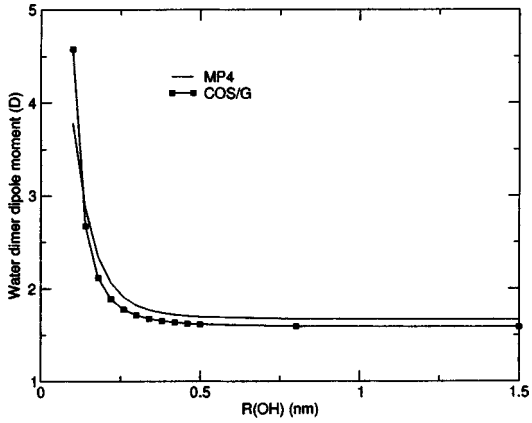

FIG. 3. Dipole moment of the water dimer as a function of R(OH) distance for the COS/G model and the *ab initio* results (Ref. 45).

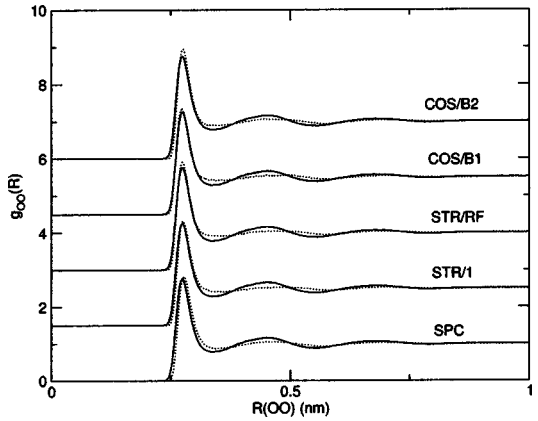

FIG. 4. Liquid phase radial distribution function at room temperature and pressure for the oxygen–oxygen pairs for the set of water models SPC, STR/1, STR/RF, COS/B1, and COS/B2 (dotted lines) along with the curves derived from experiments (solid lines) (Ref. 50). The curves are vertically shifted by 1.5 units.

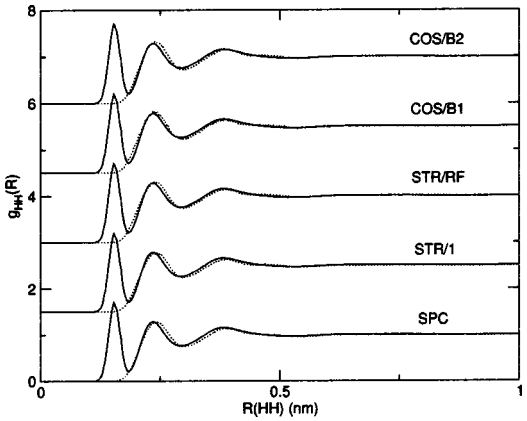

FIG. 6. Liquid phase radial distribution function at room temperature and pressure for the hydrogen–hydrogen pairs for the set of water models SPC, STR/1, STR/RF, COS/B1, and COS/B2 (dotted lines) along with the curves derived from experiments (solid lines) (Ref. 50). The curves are vertically shifted by 1.5 units.

at 300 K and 1 atm along with the radial distribution functions derived from experimental data (solid lines).[50] The general shapes of the g_{OO} (Fig. 4) of all the models are comparable to the experimentally derived one. The first peak is overestimated for all the polarizable water models. The models give slightly overstructured liquids at short distances. The coordination number can be determined by integrating $g_{OO}(R)$ over the first peak. Using the location of the first minimum in the experimental curve (0.336 nm) as the limit of integration, we obtain coordination numbers of 4.5, 4.5, 4.5, 4.6, 4.6, and 4.6, respectively for the experiment, SPC, STR/1, STR/RF, COS/B1, and COS/B2. The second and third peaks are less pronounced than in the experimentally derived curves. For g_{OH} (Fig. 5), the agreement with the experimentally derived curves is reasonable. The first peak is too high and the second peak is shifted towards shorter distances. This is compatible with the observation that the O–H bond length in our models is slightly larger than the gas-phase one, as calculated from *ab initio* methods.[52] The g_{HH} (Fig. 6) reproduces the experimental data well.

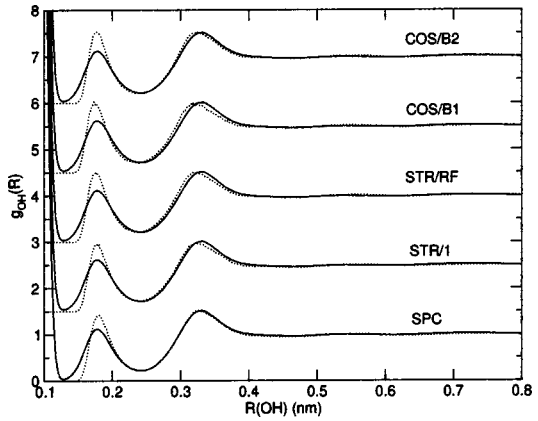

FIG. 5. Liquid phase radial distribution function at room temperature and pressure for the oxygen–hydrogen pairs for the set of water models SPC, STR/1, STR/RF, COS/B1, and COS/B2 (dotted lines) along with the curves derived from experiments (solid lines) (Ref. 50). The curves are vertically shifted by 1.5 units.

C. Dynamic properties

The self-diffusion coefficient along and the rotational relaxation times of different axes for the different models are shown in Table III. It is known that the SPC water model has a too high diffusion constant.[6] The new models all have lower diffusion constants compared to SPC, and model COS/B2 gives a value closest to the experimental one of 2.3×10^{-9} m^2 s^{-1} at 298 K and 1 atm.[51] Other polarizable water models were reported to give higher or lower diffusion constants compared to experiment, TIP4P-FQ:[9] 1.9×10^{-9} m^2 s^{-1}, POL5/TZ:[13] 1.81×10^{-9} m^2 s^{-1}, POL5/QZ:[13] 1.25×10^{-9} m^2 s^{-1}, SWRIGID-AI:[56] 3.22×10^{-9} m^2 s^{-1}, SWRIGID-ISO:[56] 3.30×10^{-9} m^2 s^{-1}. In terms of molecular rotational correlation times, generally the SPC model relaxes too fast, while STR/RF does better. We obtained improved relaxation times for COS/B1 and COS/B2. The dynamic properties of the polarizable models are in reasonable agreement with experimental data.

TABLE III. Dynamic properties of the different water models at 300 K and 1 atm. D: self-diffusion coefficient, D_x, D_y, and D_z: x, y, and z components of the self-diffusion coefficient, τ_l^α: rotational relaxation times of different molecular axes.

Model	SPC	STR/1	STR/RF	COS/B1	COS/B2	Expt
D 10^{-9} (m^2 s^{-1})	4.3	4.0	3.5	2.7	2.6	2.3 (298 K)[a]
D_x 10^{-9} (m^2 s^{-1})	4.4	4.1	3.5	2.8	2.6	
D_y 10^{-9} (m^2 s^{-1})	4.3	4.1	3.5	2.6	2.7	
D_z 10^{-9} (m^2 s^{-1})	4.2	3.8	3.6	2.7	2.5	
τ_1^{HH} (ps)	2.7	2.7	3.1	3.6	3.5	
τ_2^{HH} (ps)	1.1	1.2	1.4	1.8	1.7	2.0[b]
τ_1^{OH} (ps)	2.7	3.1	3.5	4.3	3.9	
τ_2^{OH} (ps)	1.0	1.2	1.4	1.7	1.6	1.95[c]
τ_1^{μ} (ps)	2.8	3.9	4.5	5.9	4.9	
τ_2^{μ} (ps)	0.9	1.3	1.5	1.9	1.6	1.92[d]

[a]Reference 51.
[b]Reference 53.
[c]Reference 54.
[d]Reference 55.

TABLE IV. Dielectric properties of the different water models at 300 K and 1 atm. μ: average molecular dipole moment, μ^{ind}: average induced dipole moment per molecule, G_k: finite system Kirkwood factor, g_k: infinite system Kirkwood factor, $\varepsilon(0)$: static dielectric permittivity, τ_D: Debye dielectric relaxation time, $\varepsilon(\infty)$: infinite frequency dielectric permittivity. The values of μ, μ^{ind}, and $\varepsilon(0)$ are averages over the last 1 ns of the simulations.

Model	SPC	STR/1	STR/RF	COS/B1	COS/B2	Expt
μ (D)	2.27	2.66	2.68	2.82	2.62	
μ^{ind} (D)	0	0.74	0.75	0.93	0.58	0.75[a]
$\varepsilon(0)$	65.2	142.6	126.7	170.6	121.6	78.5[b]
G_k	2.72	3.20	2.89	3.70	2.99	
g_k	2.57	4.06	3.47	5.13	3.55	2.90[c]
τ_D (ps)	6.79	6.41	12.3	25.6	14.9	8.3[d]
$\varepsilon(\infty)$	2.45	2.68	2.94	2.39	2.67	1.79,[e] 5.2[d]

[a]Reference 58.
[b]Reference 63.
[c]Reference 42.
[d]Reference 68.
[e]Reference 67.

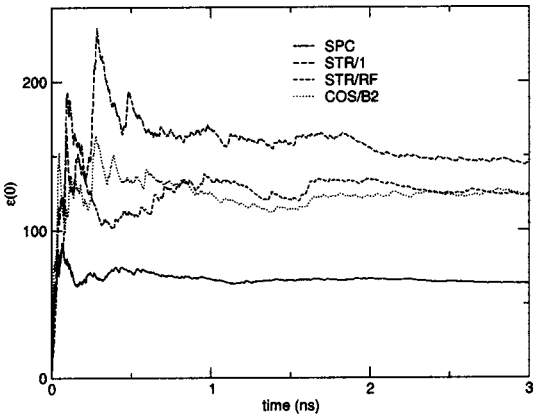

FIG. 8. Static dielectric permittivity at room temperature and pressure as a function of time for four water models. SPC: solid line, STR/1: long-dashed line, STR/RF: short-dashed line, COS/B2: dotted line.

D. Dielectric properties

The dielectric properties of the SPC, STR/1 STR/RF, COS/B1, and COS/B2 models are shown in Table IV. The convergence of the total dipole moment fluctuation in the box and the static dielectric permittivity as a function of time is displayed in Figs. 7 and 8. The additional degrees of freedom of the polarizable water models (both noniterative and self-consistent ones) make the static dielectric permittivity converge slower than for the nonpolarizable SPC model. In order to achieve convergence in the static dielectric permittivity, it is necessary to run nanosecond simulations, which was illustrated by Glättli[57] for nonpolarizable water models and by van Maaren and van der Spoel[56] for the SW polarizable water models. The obtained permittivity values $\varepsilon(0)$ are much too high. However, as is discussed below, its size is related to the average molecular dipole moment in the liquid phase.

At present the "correct" value of the liquid-state dipole moment is not clear.[13] The average dipole moment of ice was experimentally found to be 2.6 D by Coulson and Eisenberg[58] and 3.09 D by Batista *et al.*[59] recently, while the liquid-state dipole moment is suggested by *ab initio* molecular dynamics to be 2.95–3.00 D.[52] The dipole moment in ice I_h obtained from first principles calculations varies between 2.3 and 3.1 D.[60] The MCDHO *ab initio* model also predicts a dipole moment of 3.0 D.[61] However, dielectric permittivities have not been computed either for this model or from *ab initio* molecular dynamics simulations. The average dipole moment of polarizable water models in the literature varies between 2.3 to 3.1 D. According to Sprik,[62] a polarizable water model needs an average dipole moment of 2.6 D in order to reproduce the experimental static dielectric permittivity [78.5 at 298 K and 1 atm (Ref. 63)]. This conjecture was confirmed by Soetens *et al.*[64] through analyzing the relationship between the static dielectric permittivity and the average dipole moment of a series of polarizable water models. Recently, Chen *et al.*[65] inferred from their studies of polarizable water models that an average molecular dipole moment of about 2.4 and 2.5 D for a SPC-pol model or a TIP4P-pol model, respectively, would yield the correct dielectric permittivity. Our observations agree with this hypothesis. Guillot and Guissani[66] reported a model which has an average dipole moment of approximately 3.09 D. While their model seems to have a correct $\varepsilon(0)$ (78.6), this value is calculated from a much too short simulation (500 ps). Even for nonpolarizable water models (for example, SPC) at least 1 ns is necessary to get reliable $\varepsilon(0)$ values at room temperature (see Fig. 8).[57] For a polarizable water model longer simulations have been shown to be needed in order to get the average dipole in the system $\langle \mathbf{M} \rangle$ converged to zero.[56]

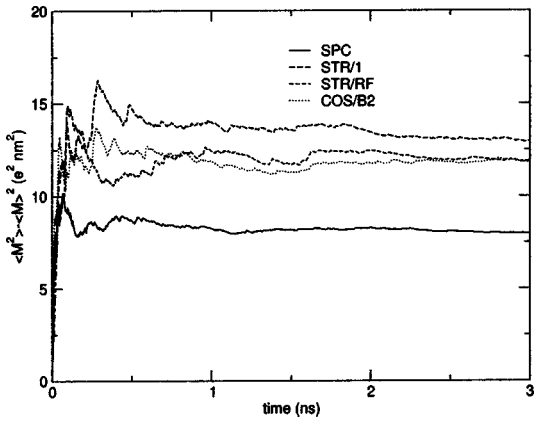

FIG. 7. Fluctuation of the total dipole moment of the box with 1331 water molecules at room temperature and pressure as a function of time for four water models. SPC: solid line, STR/1: long-dashed line, STR/RF: short-dashed line, COS/B2: dotted line.

In the literature, the induced dipole moment of water was estimated by experiments to be 0.75 D (Ref. 58) and 1.08 D with Car–Parrinello simulations,[52] whereas in the polarizable water models, the reported induced dipole moments vary extensively (POL1:[47] 0.507 D, BSV:[69] 0.999 D, CC:[69] 0.930 D, DC:[69] 0.934 D, and GG:[66] 1.29 D). STR/RF reproduced the experimentally derived induced dipole quite well (0.75 D) while the induced dipole of COS/B2 is smaller. The overestimation of the $\varepsilon(0)$ of the COS/B1 model seems to be due to its larger average dipole moment. It is not surprising that the infinite system Kirkwood factors g_k of the STR/RF and COS/B2 models are about 20% larger than the experi-

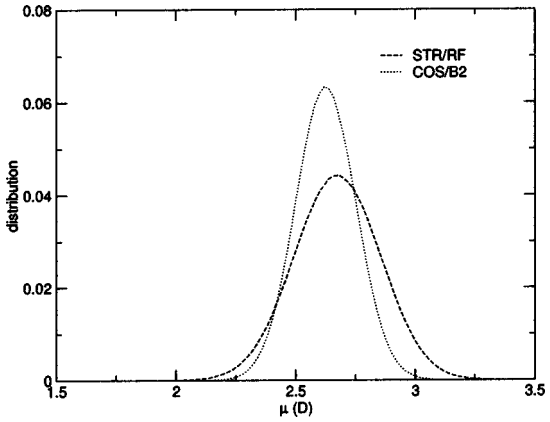

FIG. 9. The distribution of dipole moments in the liquid phase for the STR/RF (short-dashed line) and COS/B2 (dotted line) models at room temperature and pressure.

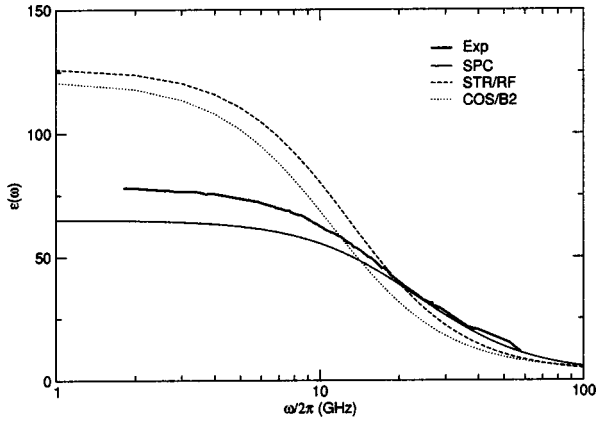

FIG. 10. The frequency dependence of the dielectric permittivity $\varepsilon(\omega)$ at room temperature and pressure for the different water models. Experimental data (thick solid line) (Ref. 68), SPC: solid line, STR/RF: short-dashed line, COS/B2: dotted line.

mental value when $\varepsilon(0)$ is already overestimated [see Eq. (22)].

A quantity which gives an estimate of the relaxation time of the hydrogen bond network is the Debye dielectric relaxation time τ_D. In contrast to SPC, the STR/RF and COS/B2 models have Debye relaxation times larger than the experimental one. As can be seen from the relation between τ_D and $\varepsilon(0)$, the overestimation of τ_D seems to be due to the overestimation of $\varepsilon(0)$ [Eq. (19)].

We have furthermore determined the distribution of the molecular dipole moment of the STR/RF and COS/B2 models (Fig. 9). The broad distributions of the dipole moment of STR/RF and COS/B2 agree well with results from *ab initio* calculations,[52] but disagree with respect to the magnetic of the dipole moment. The models have average dipole moments of 2.68 and 2.62 D, respectively, while the *ab initio* calculations suggested a value of 3.0 D. The self-consistent model differs significantly from the noniterative model, with a lower average dipole and a narrower distribution. We further evaluated the angular distribution of the induced dipoles. The mean angles between the permanent and the induced dipoles are roughly 17.4° and 15.5° for STR/RF and COS/B2, respectively, which are larger than for the SW model (12°) (Ref. 56) but smaller than for NDIS (18°–20°).[70]

The frequency dependence of the dielectric permittivity $\varepsilon(\omega)$ for the different models is shown in Fig. 10. Since the low frequency part of $\varepsilon(\omega)$ is mainly determined by the static dielectric permittivity $\varepsilon(0)$ and the Debye relaxation time [Eq. (17)], at low frequencies the SPC model underestimates $\varepsilon(\omega)$, while the polarizable water models overestimate it. The infinite frequency dielectric permittivity $\varepsilon(\infty)$ of the models can be calculated from Eq. (18) and the results are listed in Table IV. The values obtained for the models STR/RF and COS/B2 are 2.94 and 2.67, respectively, which are within the range of the experimental data of 1.79 (Ref. 67) to 5.2.[68]

E. Liquid properties at other temperatures

Densities as a function of temperature are compared with experimental data in Fig. 11. The principal feature is that the experimental density is essentially constant in the temperature interval from 258 to 288 K. SPC, STR/RF, and COS/B2 fail to reproduce this behavior and their densities decrease generally with increasing temperature. For the SPC model NPT simulations yield a temperature of maximum density at around 220 K while COS/B2 seems to have a density maximum at an even lower temperature. This behavior could be correlated to the fact, that for both of these models the optimal dimer structures (see the Sec. III F) do not reproduce the structures determined by experiments and from *ab initio* calculations. It has been suggested by Mahoney and Jorgensen[4] that a correct optimal dimer structure is important in order to achieve a proper water density profile. Also, the second peaks in the oxygen–oxygen radial distribution functions for SPC, STR/RF, and COS/B2 are less prominent compared to experimental data.

The heat of vaporization ΔH_{vap} as a function of temperature of the SPC, STR/RF, and COS/B2 models is shown in Fig. 12. The computed heats of vaporization vary linearly with temperature over a range of 150 K, which is generally consistent with the experimental data.[71] For STR/RF and COS/B2 the heat of vaporization ΔH_{vap} decreases too steeply with increasing temperature, which is also observed for the nonpolarizable TIP5P water model[4] and the polariz-

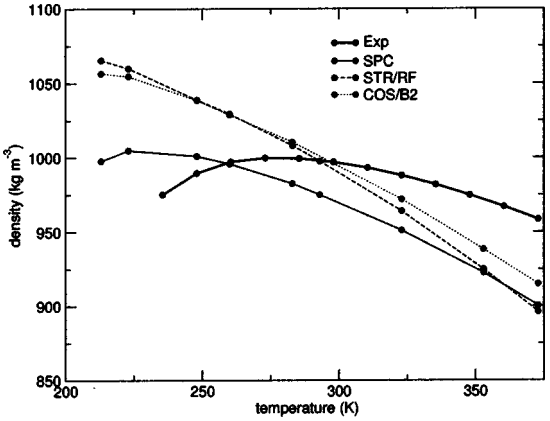

FIG. 11. Experimental and computed density for liquid water at different temperatures at 1 atm. Experimental: thick solid line, SPC: solid line, STR/RF: short-dashed line, COS/B2: dotted line.

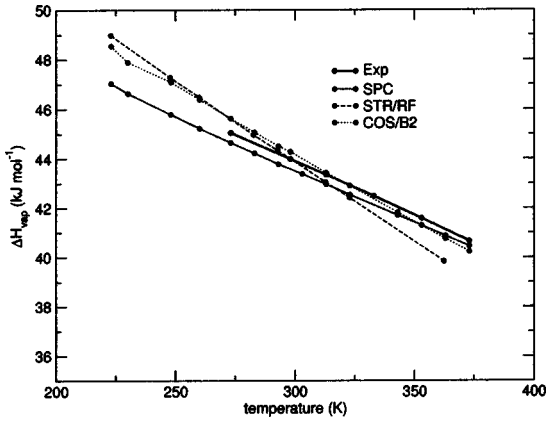

FIG. 12. Experimental and computed heat of vaporization for liquid water at different temperatures at 1 atm. Experimental: thick solid line, SPC: solid line, STR/RF: short-dashed line, COS/B2: dotted line.

able TIP4P-FQ (Ref. 9) and POL5/TZ (Ref. 13) models. This feature is reflected in the heat capacity C_p. Both STR/RF and COS/B2 generally have a too big C_p, while SPC matches the experimental values quite well (Table V). Up until now, not so many polarizable water models have been characterized with respect to C_p. Jedlovszky and Richardi[69] reported the heat capacities of the BSV,[72] CC,[70] and DC (Ref. 73) models: all of these models overestimate the C_p at 298 K and 1 atm (BSV: 114.04 J mol^{-1} K^{-1}, CC: 89.3 J mol^{-1} K^{-1}, and DC: 80.38 J mol^{-1} K^{-1} to compare to an experimental value of 75.32 J mol^{-1} K^{-1}).

TABLE V. Heat capacity C_p at constant pressure and thermal expansion coefficient α of the SPC, STR/RF, and COS/B2 models at 1 atm.

T (K)	U^{tot} (kJ mol^{-1})	C_p (kJ mol^{-1} K^{-1})	ρ (kg m^{-3})	$\alpha\ 10^{-4}$ (K^{-1})
		SPC		
298.0	−33.72		972.0	
		74.2		8.13
318.0	−32.25		956.0	
		73.7		9.99
338.0	−30.59		937.0	
		STR/RF		
298.0	−34.43		991.9	
		97.20		11.32
318.0	−32.30		969.7	
		96.20		13.22
338.0	−30.19		944.4	
		COS/B2		
298.0	−34.65		997.0	
		86.7		10.1
318.0	−32.73		977.3	
		85.2		11.0
338.0	−30.84		956.0	
		Expt[a]		
298.0		75.32	997.0	2.57
308.0		75.29	994.0	3.46
318.0		75.31	990.0	4.22
328.0		75.36	986.0	4.91
338.0		75.43	980.0	5.54

[a]References 21 and 63.

TABLE VI. Isothermal compressibility κ_T of the SPC, STR/RF, and COS/B2 models at $T=300$ K.

ρ (kg m^{-3})	Pressure (atm)	$\kappa_T 10^{-6}$ (atm^{-1})
	SPC	
947.0	−447.08	
		54.7
997.0	475.77	
		39.8
1047.0	1706.43	
	STR/RF	
947.0	−721.43	
		62.25
997.0	132.60	
		38.52
1047.0	1403.01	
	COS/B2	
947.0	−931.64	
		55.0
997.0	3.6	
		37.8
1047.0	1297.0	
	Expt[a]	
997.0	1.0	45.8

[a]Reference 21.

The thermal expansion coefficient and the isothermal compressibility are shown in Tables V and VI. Since the densities of the SPC, STR/RF, and COS/B2 models change too quickly as a function of the temperature, the coefficients of thermal expansion are overestimated (Table V). These models reproduce the experimental isothermal compressibility quite well (Table VI).

We also calculated the self-diffusion constant as a function of temperature (Fig. 13). Clearly all models reproduce the increase in the diffusion constant with increasing temperature. The COS/B2 model comes closest to the experimental values,[74,75] slightly overestimating the diffusion constant over the temperature range. A fit of the model results to the experimental data was made using the analytical function $D=D_0T^{1/2}(T/T_s-1)^{\gamma}$, which has been empirically shown

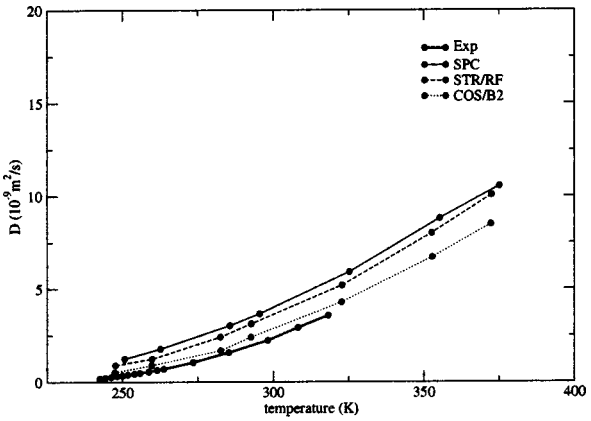

FIG. 13. Temperature dependence of the self-diffusion coefficient of liquid water at 1 atm. Experiment (Refs. 74, 75): thick solid line, SPC: solid line, STR/RF: short-dashed line, COS/B2: dotted line.

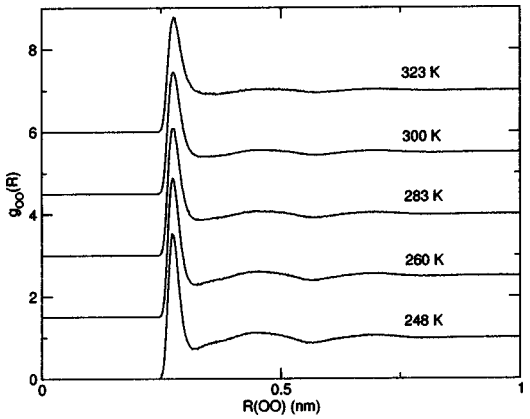

FIG. 14. Temperature dependence of the oxygen–oxygen radial distribution function for the COS/B2 model at 1 atm.

to reproduce the isobaric temperature dependence of transport properties of water.[76,77] The parameters found from the fit for the COS/B2 model are $D_0=0.78\times10^{-9}$ m^2 s^{-1} K$^{-1/2}$, $T_s=218.9$ K, and $\gamma=1.59$, which can be compared to the experimental values $D_0=0.87\times10^{-9}$ m^2 s^{-1} K$^{-1/2}$, $T_s=220$ K, and $\gamma=1.81$. The corresponding parameters for SPC are $D_0=0.77\times10^{-9}$ m^2 s^{-1} K$^{-1/2}$, $T_s=209.6$ K, and $\gamma=1.43$.

Figure 14 presents the oxygen–oxygen radial distribution functions at 248, 260, 283, 300, and 323 K. The expected loss of structure with increasing temperature is observed. However, we did not observe spontaneous crystallization in liquid COS/B2 at 248 K over a period of 2 ns.

F. Gas-phase properties

We determined the optimal dimer geometry as sketched in Fig. 15 and compared it with the one derived from high-level *ab initio* calculations.[78] These calculations constrained the monomer to be rigid (with the SPC geometry) and we performed a global conformational search. The results are shown in Table VII. In comparison with SPC, which is known to give a dimer separation which is too small and a binding energy which is too strong, STR/RF does not improve the dimer separation distance, but does decrease the binding strength by about 2 kJ mol^{-1}. For COS/B2, the dimer separation distance is slightly larger than for SPC but still too short compared to experimental data and *ab initio* calculations, while the binding energy is quite reasonable. Both STR/RF and COS/B2 are less bent (as measured by the angle ϕ) compared to experimental data, and one can assume that the less tetrahedral-like association for STR/RF and COS/B2 will negatively impact the ability to describe the liquid structure (as seen above in the oxygen–oxygen radial distribution functions). We note that the dipole moment μ^{dimer} of the dimer depends on the geometry of the dimer, and since none of the models reproduce the experimental dimer geometry, they fail to reproduce the dimer dipole moment.

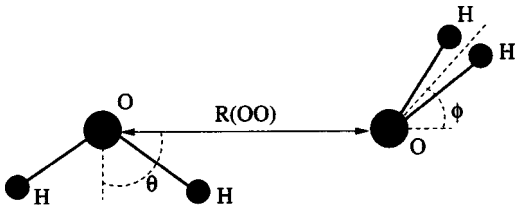

FIG. 15. Definition of the distance R(OO) and the angles ϕ and θ that determine the relative position and orientation of the monomers of the water dimer.

TABLE VII. Optimum (minimum energy) geometry, interaction energy U^{pot}, total dipole moment μ^{dimer}, and average molecular dipole moment μ^{mean} for the gas phase dimer. The geometry is defined by the O–O distance R(OO), with the angles θ and ϕ as defined in Fig. 15.

Model	$R(\text{OO})_{\text{min}}$ (nm)	θ_{min} (deg)	ϕ_{min} (deg)	U^{pot} (k mol^{-1})	μ^{dimer} (D)	μ^{mean} (D)
SPC	0.275	51.7	23.0	−27.65	3.59	2.27
STR/RF	0.272	51.7	18.0	−25.75	3.78	2.24
COS/B2	0.279	50.7	20.0	−23.29	3.76	2.26
Expt[a]	0.295	57.0	51.0	−22.60	2.60	
ab initio[b]	0.291	55.6	57.9	−21.00	2.68	2.10

[a]References 79–81.
[b]Reference 78.

The dimer energy as function of ϕ for the optimal dimer geometry using rigid monomers is presented in Fig. 16. The polarizable models yield a shallower curve than the SPC one. This feature may be responsible for the less pronounced structure of the radial distribution functions of the former models.

G. Effects of the polarization charge q_{pol} and the criterion for iterative convergence

In the STR/RF and COS/B2 models there are two model parameters that could conceivably affect the properties of the model: the polarization charge q_{pol} and the criterion for iterative convergence. The value for the polarization charge was chosen to be $-8.0\,e$. This rather big charge ensures that substantial polarization can be modelled with a relatively small displacement of the polarization charge from the polarization (oxygen atom) center. This justifies the approxima-

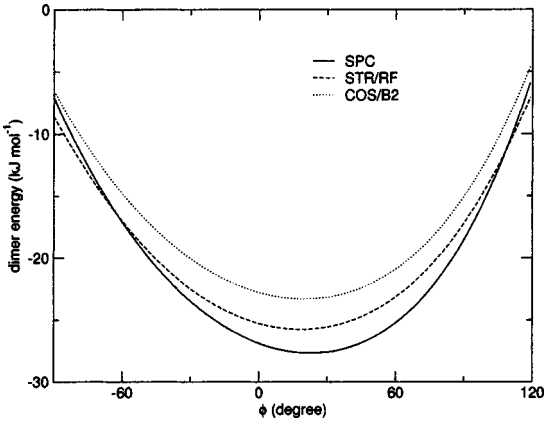

FIG. 16. Potential energy of the water dimer as a function of the angle ϕ (see Fig. 15). SPC: solid line, STR/RF: short-dashed line, COS/B2: dotted line.

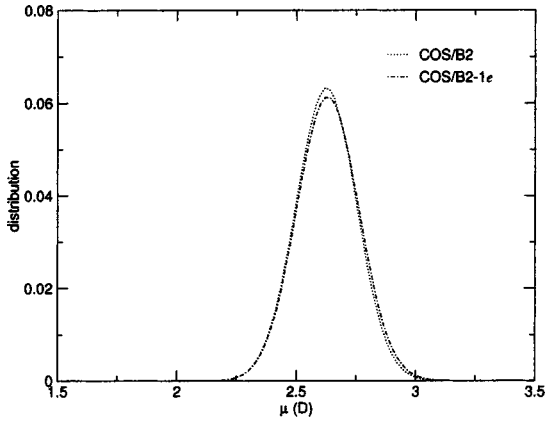

FIG. 17. The distribution of the dipole moments in the simulations of the models COS/B2 (dotted line) and COS/B2-1e (dotted–dashed line) at room temperature and pressure, which differ in the size of the polarization charge ($-8.0\ e$ and $-1.0\ e$, respectively).

tion of shifting of the forces on the polarization charge to the corresponding oxygen atom. In the COS/B2 model the average separation was 0.001 53 nm, which corresponds to one-hundredth of the smallest nonbonded oxygen–oxygen distances. Changing the value of the polarization charge will change its displacement from the oxygen atom. Straatsma and McCammon[16] observed that changing the polarization charge from $-8.0\ e$ to $-2.0\ e$ and to $-10.0\ e$, however, does not noticeably alter the radial distribution functions of the STR/1 model. The criterion for the iterative convergence was chosen to be about k_BT at 300 K in every component [Eq. (6)]. Simulations in which the COS/B2 model had a polarization charge of $-1.0\ e$ (COS/B2-1e) and others in which the criteria for iterative convergence were set to 1 and 5 kJ mol^{-1} (COS/B2-1 kJ and COS/B2-5 kJ), respectively were performed to investigate the effects of variation of the two parameters. One should note that the COS/B2 model was parametrized with a polarization charge of $-8.0\ e$ and a convergence criterion of 2.5 kJ mol^{-1}.

As for the thermodynamic properties from 3 ns simulations we did not see much difference between COS/B2 and COS/B2-1e (the difference in the potential energy and density are about 2% and 1%, respectively). The dipole moment distributions, shown in Fig. 17, are very similar. In COS/B2-1e, the average dipole is slightly bigger than in COS/B2. The average angle between the induced dipole and the permanent dipole is approximately equal to 15.5° for both models and the average separations of the polarization charges are, respectively, 0.012 373 nm and 0.001 53 nm (the ratio between them is close to 8). However, the fluctuation of the total potential energy of COS/B2-1e is about 5% larger and the actual temperature is 1 K higher than for the COS/B2 model. As for the structural properties, we did not observe any noticeable difference in the radial distribution functions in the two simulations.

In the calculations for COS/B2 − 1 kJ, COS/B2, and COS/B2 − 5 kJ, the average number of iteration steps needed to obtain converged solutions is, respectively, 3, 2.1, and 2. The properties of 500 ps simulations are listed in Table VIII. The average temperature of the COS/B2 − 1 kJ simulation is about 4.6 K higher than the bath temperature, even though in this simulation more iteration steps are needed and the convergence criterion is more strict. We did not observe obvious differences in structural properties.

IV. CONCLUSION

In this work, the COS model was further investigated to develop both a noninterative model and a self-consistent model based on the SPC geometry with one additional interaction center. The thermodynamic properties, static dielectric permittivity, structural properties, and dynamic properties of the models were examined through molecular dynamics simulations. It should be noted that the simulations were performed with a larger system and for considerably longer time periods than those of earlier work, which reduces finite size effects and improves averaging and convergence.

The COS model circumvents the complex evaluation of dipole–dipole forces, since all the electrostatic interactions are point-charge interactions. Thus it is very straightforwardly combined with different methods of treating the long-range electrostatic interactions and can be extended to standard bimolecular force fields. Both STR/RF and COS/B2 reproduce the experimental heat of vaporization, density, self-diffusion coefficient, and rotational correlation times at 300 K and 1 atm.

The STR/RF and COS/B2 models were optimized for reproducing the liquid water properties rather than gas-phase cluster properties, and neither STR/RF nor COS/B2 give correct dimer properties, which may relate to the fact they do not show a pronounced structure beyond the first solvation shell in the liquid phase. The dielectric properties of both models are not perfect. Both of them overestimate the static dielectric permittivity. From our results we infer that the average molecular dipole moment of about 2.4–2.5 D would be desirable for COS models to yield the correct dielectric permittivity. However, within the framework of three atomic-centered models with SPC geometry and one additional interaction site, the STR/RF and COS/B2 models are optimal

TABLE VIII. Properties of the model COS/B2 as function of the polarization convergence criterion at 300 K and 1 atm together with the root-mean-square fluctuation in parentheses. The different criteria used are discussed in Sec. III G.

Model	T (K)	Pressure (atm)	U^{pot} (kJ mol^{-1})	ρ (kg m^{-3})	μ (D)
COS/B2-1 kJ	304.65(3.64)	−2.49(238.21)	−41.63(0.14)	992.4(4.67)	2.63
COS/B2	302.73(3.41)	12.79(238.11)	−41.72(0.14)	992.6(4.41)	2.63
COS/B2-5 kJ	302.38(3.52)	−2.92(237.17)	−41.73(0.15)	991.9(4.58)	2.63

compromises when aiming at agreement with a variety of experimentally determined properties of liquid water.

In the STR/RF and COS/B2 models, the molecular polarizability was used instead of atom-centered polarizabilities. Caldwell *et al*.[47] found that the use of atom-centered polarizabilities rather than the molecular one appeared to be an improvement in the studies of the liquid and ionic solutions, which is also suggested by Jedlovsky and Richardi.[69] The extra degrees of freedom however complicate the model. Another possibility would be to allow for molecular flexibility, which has a fairly big effect on the thermodynamic properties and dielectric properties.[56] It seems that polarizable water models based on three atom-centered geometry cannot produce the correct optimal dimer structure (especially regarding the orientation of the two water monomers).[56] One possibility to improve this would be to incorporate a virtual atom such as in the TIP4P water model, which would increase the computation cost.

In this study, we have investigated whether a polarizable water model based on the COS scheme could be developed that reproduces a variety of properties of liquid water at room temperature. The variation of different model parameters gave insight into relationships between these and the different properties. In addition, the behavior of the polarizable water models as function of temperature was investigated. Although viable polarizable models were derived, they are not wholly satisfactory, since not all water properties are accurately modelled. Therefore, further work on polarizable models, their comparison and their application to reproduce a variety of structural, thermodynamic, dielectric, and dynamic properties of water in the condenses phase is needed.

ACKNOWLEDGMENTS

Financial support was obtained from the Schweizer Nationalfonds, Project No. 2000-063590.00, which is gratefully acknowledged.

[1] H. J. C. Berendsen, J. P. M. Postma, W. F. van Gunsteren, and J. Hermans, in *Intermolecular Forces*, edited by B. Pullman (Reidel, Dordrecht, 1981), p. 331.
[2] H. J. C. Berendsen, J. R. Grigera, and T. P. Straatsma, J. Phys. Chem. **91**, 6269 (1987).
[3] W. L. Jorgensen, J. Chandrasekhar, J. D. Madura, R. W. Impey, and M. L. Klein, J. Chem. Phys. **79**, 926 (1983).
[4] M. W. Mahoney and W. L. Jorgensen, J. Chem. Phys. **112**, 8910 (2000).
[5] M. W. Mahoney and W. L. Jorgensen, J. Chem. Phys. **114**, 363 (2001).
[6] A. Glättli, X. Daura, and W. F. van Gunsteren, J. Chem. Phys. **116**, 9811 (2002).
[7] L. X. Dang, J. E. Rice, J. Caldwell, and P. A. Kollman, J. Am. Chem. Soc. **113**, 2481 (1991).
[8] H. A. Halgren and W. Damm, Curr. Opin. Struct. Biol. **11**, 236 (2001).
[9] S. W. Rick, S. J. Stuart, and B. J. Berne, J. Chem. Phys. **101**, 6141 (1994).
[10] S. W. Rick, J. Chem. Phys. **114**, 2276 (2001).
[11] H. A. Stern, G. A. Kaminski, J. L. Banks, R. H. Zhou, B. J. Berne, and R. A. Friesner, J. Phys. Chem. **103**, 4730 (1999).
[12] W. F. Murphy, J. Chem. Phys. **67**, 5877 (1977).
[13] H. A. Stern, F. Rittner, B. J. Berne, and R. A. Friesner, J. Chem. Phys. **115**, 2237 (2001).
[14] J. A. Caldwell and P. A. Kollman, J. Phys. Chem. **99**, 6208 (1995).
[15] D. van Belle, M. Froeyen, G. Lippens, and S. J. Wodak, Mol. Phys. **77**, 239 (1992).
[16] T. P. Straatsma and J. A. McCammon, Mol. Simul. **5**, 181 (1990).
[17] W. F. van Gunsteren, S. R. Billeter, A. A. Eising, P. H. Hünenberger, P. Krüger, A. E. Mark, W. R. P. Scott, and I. G. Tironi, *Biomolecular Simulation: The GROMOS Manual and User Guide* (vdf Hochschulverlag, ETH Zürich, Switzerland, 1996).
[18] W. R. P. Scott, P. H. Hünenberger, I. G. Tironi, A. E. Mark, S. R. Billeter, J. Fennen, A. E. Torda, T. Huber, P. Krüger, and W. F. van Gunsteren, J. Phys. Chem. **103**, 3596 (1999).
[19] J. P. Ryckaert, G. Ciccotti, and H. J. C. Berendsen, J. Comput. Chem. **23**, 327 (1977).
[20] H. J. C. Berendsen, J. P. M. Postma, W. F. van Gunsteren, A. DiNola, and J. R. Haak, J. Chem. Phys. **81**, 3684 (1984).
[21] G. S. Kell, J. Chem. Eng. Data **12**, 66 (1967).
[22] M. Neumann, J. Chem. Phys. **82**, 5663 (1985).
[23] I. G. Tironi, R. Sperb, P. E. Smith, and W. F. van Gunsteren, J. Chem. Phys. **102**, 6199 (1995).
[24] B. A. Luty and W. F. van Gunsteren, J. Phys. Chem. **100**, 2581 (1996).
[25] I. G. Tironi, B. A. Luty, and W. F. van Gunsteren, J. Chem. Phys. **106**, 6068 (1997).
[26] P. H. Hünenberger and J. A. McCammon, J. Chem. Phys. **110**, 1856 (1999).
[27] P. H. Hünenberger and J. A. McCammon, Biophys. Chem. **78**, 69 (1999).
[28] W. Weber, P. H. Hünenberger, and J. A. McCammon, J. Phys. Chem. **104**, 3668 (2000).
[29] T. M. Nymand and P. Linse, J. Chem. Phys. **112**, 6386 (2000).
[30] R. Walser, P. H. Hünenberger, and W. F. van Gunsteren, Proteins **44**, 509 (2001).
[31] B. Oliva and P. H. Hünenberger, J. Chem. Phys. **116**, 6898 (2002).
[32] J. P. M. Postma, Ph.D. thesis, Rijksuniversiteit, Groningen, The Netherlands, 1985.
[33] M. P. Allen and D. J. Tildesley, *Computer Simulation of Liquids* (Clarendon, Oxford, 1987).
[34] W. G. Rothschild, *Dynamics of Molecular Liquids* (Wiley, New York, 1984).
[35] B. J. Berne and R. Pecora, *Dynamic Light Scattering* (Wiley, New York, 1976).
[36] G. R. Fleming, *Chemical Application of Ultrafast Spectroscopy* (Oxford University Press, New York, 1986).
[37] M. Neumann, Mol. Phys. **50**, 841 (1983).
[38] D. van der Spoel, P. J. van Maaren, and H. J. C. Berendsen, J. Chem. Phys. **108**, 10220 (1998).
[39] M. Neumann, O. Steinhauser, and G. S. Pawley, Mol. Phys. **52**, 97 (1984).
[40] P. Debye, *Polar Molecules* (Chemical Catalog, New York, 1929).
[41] J. T. Kindt and C. A. Schmuttenmaer, J. Phys. Chem. **100**, 10373 (1996).
[42] M. Neumann, Mol. Phys. **57**, 97 (1986).
[43] I. G. Tironi and W. F. van Gunsteren, Mol. Phys. **83**, 381 (1994).
[44] K. A. Motakabbir and M. Berkowitz, J. Phys. Chem. **94**, 8359 (1990).
[45] M. Alfredsson, J. P. Brodholt, K. Hermanson, and R. Vallauri, Mol. Phys. **94**, 873 (1998).
[46] I. M. Svishchev, P. G. Kusalik, J. Wang, and R. J. Boyd, J. Chem. Phys. **105**, 4742 (1996).
[47] J. Caldwell, L. X. Dang, and P. A. Kollman, J. Am. Chem. Soc. **112**, 9144 (1990).
[48] L. X. Dang, J. Chem. Phys. **97**, 2659 (1992).
[49] D. Eisenberg and W. Kauzmann, *The Structure and Properties of Water* (Oxford University Press, London, 1969).
[50] A. K. Soper, Chem. Phys. **258**, 121 (2000).
[51] K. Krynicki, C. D. Green, and D. W. Sawyer, Faraday Discuss. Chem. Soc. **66**, 199 (1978).
[52] P. L. Silvestrelli and M. Parrinello, J. Chem. Phys. **111**, 3572 (1999).
[53] B. Halle and H. Wennerström, J. Chem. Phys. **75**, 1928 (1981).
[54] R. Ludwig, Chem. Phys. **195**, 329 (1995).
[55] M. S. P. Sansom, I. D. Kerr, J. Breed, and R. Sankararanakrishnan, Biophys. J. **70**, 693 (1996).
[56] P. J. van Maaren and D. van der Spoel, J. Phys. Chem. **105**, 2618 (2001).
[57] A. Glättli, Diplomarbeit, ETH Zürich, Switzerland, 2000.
[58] C. A. Coulson and D. Eisenberg, Proc. R. Soc. London, Ser. A **291**, 445 (1966).
[59] E. R. Batista, S. S. Xantheas, and H. Jonsson, J. Chem. Phys. **109**, 4546 (1998).
[60] E. R. Batista, S. S. Xantheas, and H. Jonsson, J. Chem. Phys. **111**, 6011 (1999).
[61] H. Saint-Martin, J. Hernández-Cobos, M. I. Bernal-Uruchurtu, I. Ortega-Blake, and H. J. C. Berendsen, J. Chem. Phys. **113**, 10899 (2000).
[62] M. Sprik, J. Chem. Phys. **95**, 9 (1995).
[63] *Handbook of Chemistry and Physics*, 56th ed., edited by R. C. Weast (CRC, Boca Raton, 1976).

[64] J. C. Soetens, M. T. C. M. Costa, and C. Millot, Mol. Phys. **94**, 577 (1998).
[65] B. Chen, J. H. Xing, and J. I. Siepmann, J. Phys. Chem. **104**, 2391 (2000).
[66] B. Guillot and Y. Guissani, J. Chem. Phys. **114**, 6720 (2001).
[67] A. D. Buckingham, Proc. R. Soc. London, Ser. A **238**, 235 (1956).
[68] U. Kaatze, J. Chem. Eng. Data **34**, 371 (1989).
[69] P. Jedlovszky and J. Richardi, J. Chem. Phys. **110**, 8019 (1999).
[70] A. A. Chialvo and P. T. Cummings, J. Chem. Phys. **105**, 8274 (1996).
[71] J. A. Riddick, W. B. Bunger, and T. K. Sakano, *Techniques of Chemistry, Vol. II: Organic Solvents, Physical Properties and Methods of Purification*, 4th ed. (Wiley, New York, 1986).
[72] J. Brodholt, M. Sampli, and R. Vallauri, Mol. Phys. **86**, 149 (1995).
[73] L. X. Dang and T. M. Chang, J. Chem. Phys. **106**, 8149 (1997).
[74] K. T. Gillen, D. C. Douglass, and M. J. R. Hoch, J. Chem. Phys. **57**, 5117 (1972).
[75] R. Mills, J. Phys. Chem. **77**, 685 (1973).
[76] F. X. Prielmeier, E. W. Lang, R. J. Speedy, and H. D. Lüdemann, Phys. Rev. Lett. **59**, 1128 (1987).
[77] R. J. Speedy and C. A. Angell, J. Chem. Phys. **65**, 851 (1976).
[78] W. Klopper, J. G. C. M. van Duijneveldt-van de Rijdt, and F. B. van Duijneveldt, Phys. Chem. Chem. Phys. **2**, 2227 (2000).
[79] J. G. C. M. van Duijneveldt-van de Rijdt and F. B. van Duijneveldt, J. Chem. Phys. **97**, 5019 (1992).
[80] J. A. Odutola and T. R. Dyke, J. Chem. Phys. **72**, 5062 (1980).
[81] L. A. Curtiss, D. J. Frurip, and M. J. Blander, J. Chem. Phys. **71**, 2703 (1979).